

Synergistic interfacial engineering of a S-scheme ZnO/In₂S₃ photocatalyst with S–O covalent bonds: A dual-functional advancement for tetracycline hydrochloride degradation and H₂ evolution

Yating Ai ^{a,b}, Jiajie Hu ^c, Xianqiang Xiong ^{a,*}, Sónia A.C. Carabineiro ^d, Yuesheng Li ^e, Nikolay Sirotkin ^f, Alexander Agafonov ^f, Kangle Lv ^{g,*}

^a School of Pharmaceutical and Chemical Engineering, Taizhou University, Jiaojiang 318000, China

^b College of Food and Pharmaceutical Engineering, Nanjing Normal University, Nanjing 210023, China

^c Zhejiang Xianju Pharmaceutical Co., Ltd., Taizhou 318000, China

^d LAQV-REQUIMTE, Department of Chemistry, NOVA School of Science and Technology, Universidade NOVA de Lisboa, Caparica 2829-516, Portugal

^e School of Nuclear Technology and Chemistry & Biology, Hubei Key Laboratory of Radiation Chemistry and Functional Materials, Hubei University of Science and Technology, Xianning 437000, China

^f G.A. Krestov Institute of Solution Chemistry of the Russian Academy of Sciences, Ivanovo 153045, Russia

^g College of Resources and Environment, South-Central Minzu University, Wuhan 430074, China



ARTICLE INFO

Keywords:

In₂S₃
ZnO
Photocatalysis
S-scheme heterojunction
Interface interactions

ABSTRACT

Efficient interfacial charge transfer and robust interface interactions are crucial to achieve superior spatial separation of carriers and develop advanced heterogeneous photocatalysts. This study describes the synthesis of a novel S-scheme heterojunction of ZnO/In₂S₃, with S–O covalent bonds, achieved through a hydrothermal method. The optimized heterojunction shows exceptional photocatalytic activity, achieving a H₂ generation rate of 2488 μmol g⁻¹ h⁻¹ and a degradation efficiency of 86 % for tetracycline hydrochloride (TCH) within 2 h. These values surpass those of In₂S₃ alone by 35 and 1.4 times, respectively. Various techniques, including electron spin resonance, X-ray photoelectron spectroscopy, Kelvin probe force microscopy and density functional theory calculations confirm the S-scheme heterojunction. The establishment of a chemical S–O bond between In₂S₃ and ZnO facilitates an atomic level interfacial pathway, enabling efficient transportation of interfacial electrons.

1. Introduction

The fast expansion of the global economy and recent societal advancements present significant challenges in addressing environmental concerns and managing energy crises [1]. Semiconductor photocatalysis technology emerges as a promising solution for harnessing renewable solar energy to facilitate clean hydrogen production, thereby potentially mitigating contemporary energy and environmental challenges [2]. The degradation of organic pollutants requires highly oxidative holes, while efficient hydrogen production demands highly reducing electrons. Therefore, the selected semiconductor photocatalyst must exhibit both high oxidation potential and a robust reduction capacity. However, achieving these dual characteristics in a single photocatalyst remains a significant challenge [3,4]. Individual photocatalysts often encounter limitations, such as weak redox potential, accelerated electron-hole pair

recombination, and reduced efficiency in photon utilization. Hence, it is imperative to explore innovative approaches aimed at enhancing the photocatalytic efficiency of individual semiconductor materials.

In recent years, the exploration of 2D materials for achieving efficient and cost-effective photocatalysis in various reactions has been attracting significant attention, due to their unique physicochemical properties [5]. Among these materials, indium sulfide (In₂S₃) stands out as a promising 2D candidate with distinctive properties that confer unique advantages for specific applications when compared to other materials. In₂S₃ demonstrates excellent chemical stability and good thermal robustness, making it highly suitable for photocatalytic applications [6]. Its ultrathin configuration allows easy electron and hole transfer from the interior to the surface, while its solid specific surface area enhances the adsorption and desorption of reactants and products [6]. Additionally, its narrow bandgap, ranging from 2.0 to 2.3 eV,

* Corresponding authors.

E-mail addresses: 11337061@zju.edu.cn (X. Xiong), lvkangle@mail.scuec.edu.cn (K. Lv).

ensures efficient absorption of visible light [7]. Moreover, the negative conduction band (CB) potential (-0.56 to -1.23 V vs. NHE) provides a strong reduction ability [7,8], satisfying the thermodynamic prerequisites for the reduction of H_2O to H_2 . However, the widespread utilization of In_2S_3 as a photocatalyst faces challenges due to its substantial electron-hole recombination rate and low valence band position, limiting its oxidation capability [9]. Several strategies have been employed to overcome these limitations and enhance the photocatalytic efficiency of In_2S_3 . These strategies include constructing heterojunctions [10], introducing defects [11], controlling morphology [12] and incorporating co-catalysts [13]. Among these approaches, the construction of heterojunctions through the integration of two semiconductors, such as $\text{In}_2\text{S}_3/\text{TiO}_2$ [14], $\text{In}_2\text{S}_3/\text{Zn}_3\text{In}_2\text{S}_6$ [15], $\text{In}_2\text{O}_3/\text{In}_2\text{S}_3$ [16], and $\text{In}_2\text{S}_3/\text{Bi}_2\text{WO}_6$ [17], has demonstrated significant advantages in developing highly efficient photocatalytic systems. These benefits include enhanced photon capture, augmented charge dissociation, and robust redox capabilities.

In 2019, Yu et al. proposed an innovative S-scheme heterojunction structure [18], distinct from conventional type II heterojunction structures. The unique characteristics of the S-scheme heterojunction arise from its interface, which establishes a distinctive charge migration route and notable photo-redox capability, driven by the internal electric field (IEF) [19,20]. This heterojunction structure includes an oxidation-type semiconductor (OS) and a reduction-type semiconductor (RS), promoting accelerated electron recombination in the OS's CB with holes in the RS's VB at their interface [21,22]. Consequently, the retention of strongly reducing electrons and highly oxidizing holes enhances efficient carrier separation, and improves their powerful redox capacity for photoreduction and photodegradation [23]. The effective design of a S-scheme heterojunction needs to meet two essential conditions: (1) achieving an appropriate band structure where the VB, Fermi level, and CB of the RS exceed those of the OS, and (2) establishing a closely aligned and wide contact interface that facilitates efficient charge carrier transportation. Hence, the fabrication of a S-scheme heterojunction utilizing In_2S_3 , featuring a negative CB potential, requires the incorporation of a semiconductor with a significant oxidation potential. This ensures the preservation of a robust oxidation-reduction capability, which is crucial for the success of the designed heterojunction.

Zinc oxide (ZnO) is a semiconductor recognized for its elevated oxidation potential that has become prominent in photocatalytic applications due to its non-toxicity, abundance, superior electron mobility, and robust oxidation capacity [24]. With a VB potential of ~ 2.7 V vs. NHE, ZnO acts as an oxidative semiconductor when coupled with high CB position semiconductors, such as $\text{g-C}_3\text{N}_4$, CdS , ZnIn_2S_4 , and In_2O_3 [25–28]. This combination results in the creation of S-scheme photocatalysts with exceptional photocatalytic activity.

Applying these principles, the combination of RS In_2S_3 and OS ZnO is expected to establish an effective S-scheme photocatalytic system, facilitating efficient charge separation and maintaining highly oxidative holes and reductive electrons for pollutant degradation and H_2 production. However, the $\text{ZnO}/\text{In}_2\text{S}_3$ heterojunction designed in the S-scheme configuration may face two common challenges observed in other S-scheme systems. Firstly, achieving chemical bond-level interfacial interactions for high charge transport efficiency remains a remarkable challenge [29,30]. Secondly, the precise mechanics of charge transfer across the interfaces of the composites are not yet fully understood. Therefore, it is crucial to develop chemically bonded $\text{ZnO}/\text{In}_2\text{S}_3$ S-scheme heterojunctions that accelerate effective charge carrier transport and gain a comprehensive understanding of the associated charge transfer mechanism.

In this study, we successfully synthesized a novel S-scheme heterojunction composite of $\text{ZnO}/\text{In}_2\text{S}_3$ through a one-step hydrothermal method. A distinctive aspect of the hydrothermal growth process is the formation of S-O chemical bonds between the oxygen atoms on the ZnO surface and the sulfur atoms on the In_2S_3 surface. This chemical bonding during synthesis resulted in the creation of closer and more intimate

heterojunctions between ZnO and In_2S_3 , establishing an atomic-level interfacial channel. This unique feature facilitated efficient electron transfer along a charge migration pathway, characteristic of the S-scheme configuration. As a consequence of the well-established S-scheme heterojunction, the 40 %- $\text{ZnO}/\text{In}_2\text{S}_3$ composite demonstrated remarkable photocatalytic activity in the degradation of TCH, achieving an impressive degradation rate of 86 % within 120 min. Furthermore, the rate of hydrogen production of the composite photocatalyst, consisting of 30 % ZnO and In_2S_3 , reached an outstanding $2488 \mu\text{mol g}^{-1} \text{ h}^{-1}$. This represented a substantial 35-fold enhancement compared to the performance of In_2S_3 alone.

To unravel the reasons behind this substantial increase, a thorough investigation was carried out using advanced characterization techniques such as transient-state photoluminescence (PL), electron paramagnetic resonance (EPR) measurements, *in situ* atomic force microscopy with Kelvin probe force microscopy (AFM-KPFM), *in situ* X-ray photoelectron spectroscopy (XPS) and density functional theory (DFT) calculations. Notably, both *ex situ* and *in situ* XPS, along with theoretical calculations, revealed the intricate electronic interaction between ZnO and In_2S_3 . Moreover, AFM-KPFM provided visual insights into the migration routes of photogenerated charges and surface potential changes within the $\text{ZnO}/\text{In}_2\text{S}_3$ composite under illumination. In light of these findings, this work emphasizes the important role of intimate interface interactions and rapid charge separation in advancing the fields of environmental preservation and energy production.

2. Experimental

2.1. Synthesis of In_2S_3 (IS)

Aiming at the synthesis of In_2S_3 microspheres, a mixture containing 1.0 mmol of $\text{InCl}_3 \cdot 4\text{H}_2\text{O}$, 2.0 mmol of thioacetamide (TAA), and 1.7 mmol of urea was prepared. This mixture was dispersed in a solution consisting of 50 mL of ethanol and water in a 1:1 vol ratio. After stirring at ambient temperature for 1 h, the solution was transferred into a 100 mL PTFE-lined autoclave. The autoclave process was conducted at 180°C for 12 h. After naturally cooling to room temperature, the solution was centrifuged and washed 3 times using deionized water and ethanol. This procedure yielded a dark yellow sample. The material was then vacuum-dried at 60°C for 12 h, yielding In_2S_3 microspheres.

2.2. Preparation of the $\text{ZnO}/\text{In}_2\text{S}_3$ (ZO/IS) heterojunction

Scheme 1 outlines the synthetic procedure for the preparation of the ZO/IS composites. ZnO nanoparticles (ZO NPs) were purchased directly from Aladdin Biochemical Technology Co., Ltd. Varying quantities of ZO NPs were introduced into a solution of 50 mL ethanol and water (in a 1:1 vol ratio). This solution, containing 1.0 mmol $\text{InCl}_3 \cdot 4\text{H}_2\text{O}$, 2.0 mmol TAA, and 1.7 mmol urea, was stirred for 1 h. The resulting mixture was then transferred to an autoclave coated with polytetrafluoroethylene and held at 180°C for 12 h. The precipitate was extensively washed with ethanol and deionized water before being dried under vacuum at 60°C for 12 h. The resulting composite materials were denoted as $x\%-\text{ZO}/\text{IS}$, with $x\%$ representing the weight ratio of ZnO to In_2S_3 .

Additional information on materials, characterizations, photocatalytic antibiotic degradation experiments, photocatalytic hydrogen evolution tests, electrochemical measurements, and DFT calculations can be found in [Supporting Information](#).

3. Results and discussion

3.1. Characterization of photocatalysts

Samples were analyzed by scanning electron microscopy (SEM) to examine their microscopic morphology. In [Fig. 1a](#), the microflower-like morphology of pure IS is evident, comprising multiple nanoscale sheets



Scheme 1. Illustration of the preparation process of ZO/IS.

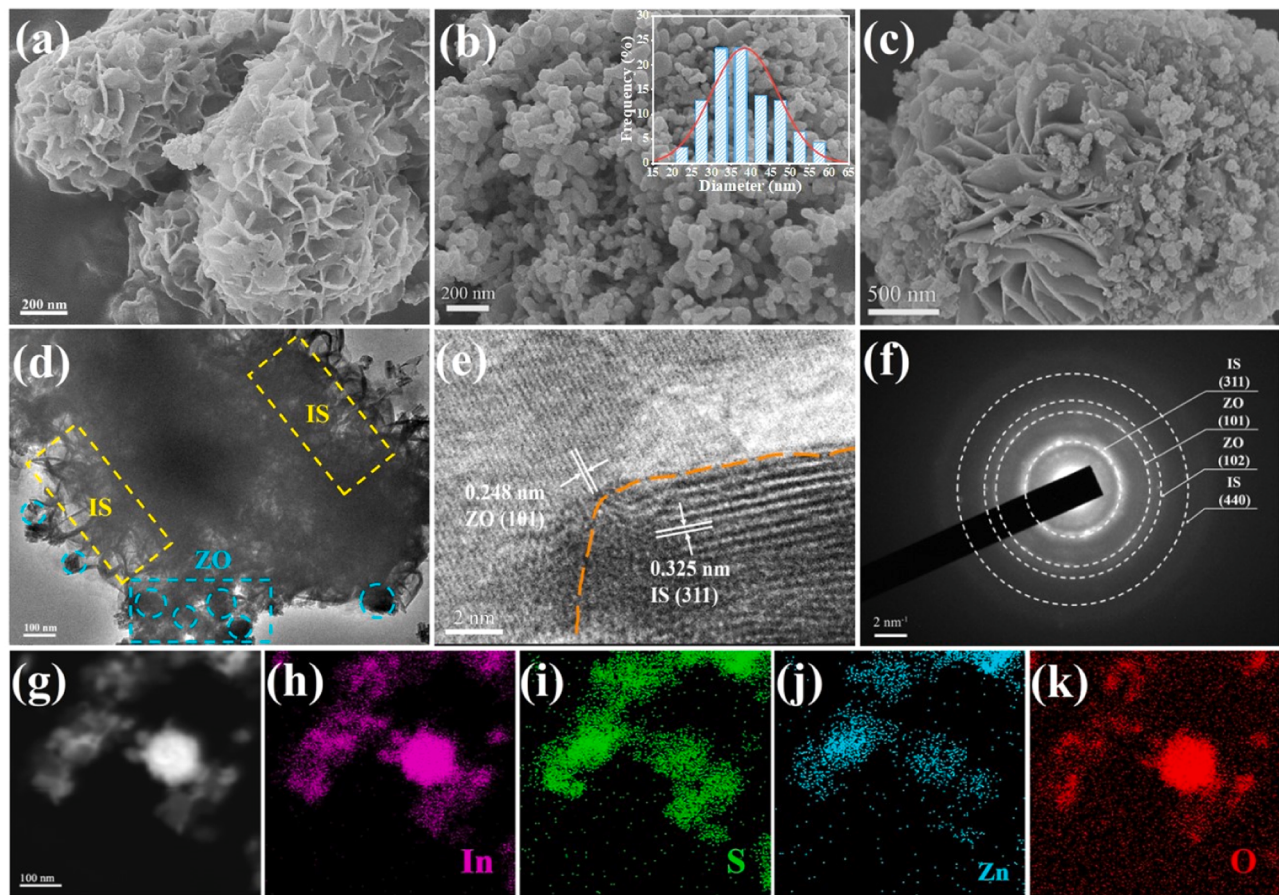


Fig. 1. SEM images of (a) IS, (b) ZO (with respective particle size distribution histogram) and (c) 40 %-ZO/IS. (d) TEM, (e) HRTEM, (f) SAED and (g-k) elemental mapping images of 40 %-ZO/IS.

with a broad size distribution (diameter: 0.6–1 μm). Fig. 1b reveals the irregular nanoparticle structure of ZO, consisting of particles ranging in size from 20 to 60 nm see inset. In Fig. 1c, the 40 %-ZO/IS sample displays a morphology similar to that of IS, with ZO NPs randomly dispersed on the IS surface, indicating favorable interactions between the two components. Both IS and 40 %-ZO/IS (Figs. 1a and c) display lamellar structures arranged in a flower-like pattern, suggesting that the incorporation of ZO has minimal impact on the IS morphology. The presence of 2D IS nanosheets significantly reduces ZO aggregation, thereby decreasing the surface energy of ZO nanoparticles and enhancing the accessibility of additional active sites. Fig. S1 displays SEM images of 20 %-ZO/IS, 30 %-ZO/IS and 40 %-ZO/IS, showing an increase in the number of small particles attached to the ZO/IS surface as ZO content increases.

Transmission electron microscopy (TEM) and high-resolution TEM (HRTEM) techniques were employed for a comprehensive examination of the ZO/IS heterostructures. This approach facilitated the detailed analysis of microscopic structures, precise interfacial interactions, and lattice parameter measurements. Fig. 1d shows a TEM image of the ZO/IS composite, revealing a unique flower-like structure characterized by the random dispersion of nanoparticles, a characteristic attributed to the presence of ZO. The successful synthesis of the heterojunction photocatalyst is evidenced by the effective encapsulation of nanoscale ZO particles on the surface of the IS micro-flowers, resulting in a strong interconnection. HRTEM analysis (Fig. 1e) further supports this observation, enabling precise measurement of lattice spacings. The intimate association between IS and ZO is supported by the observed lattice fringe spacings: 0.325 nm for the (311) plane of IS and 0.248 nm for the

(101) plane of ZO. The selected area electron diffraction (SAED) pattern of the 40 %–ZO/IS composite depicted in Fig. 1f provides additional evidence of the presence of both ZO and IS in the composite. The diffraction pattern displays pronounced spots, attributed to the IS and ZO phases. The IS phase is characterized by the (311) and (440) planes, with lattice fringe measurements of 0.325 nm and 0.191 nm, respectively. The (101) and (102) crystallographic planes of ZO are discernible, exhibiting lattice fringes of 0.248 nm and 0.191 nm, respectively. Furthermore, the mapping images (Figs. 1g–k) provide compelling evidence of the homogeneous dispersion of the indium (In), sulfur (S), zinc (Zn), and oxygen (O) elements throughout the composite structure.

The phase composition and crystal structure of the samples were analyzed using X-ray diffraction (XRD). Fig. 2a illustrates the XRD diffractograms of the ZO/IS heterojunction photocatalysts, synthesized with different quantities of ZO. For IS, the diffraction peaks observed at 2θ values of 27.4°, 28.7°, 33.2°, 43.6°, 47.7°, 56.1°, 59.4°, 66.7°, 69.9°, and 76.9° correspond to the cubic crystal structure's (311), (222), (400), (511), (440), (533), (444), (731), (800), (751) planes (JCPDS no. 84–1385), respectively [31]. The diffraction peaks detected at 31.2°, 36.8°, 38.5°, 44.8°, 55.6°, 59.3°, and 65.2° can be attributed to the cubic ZO's (100), (002), (101), (102), (110), (103), (112) planes (JCPDS no. 36–1451), respectively [32]. With an increase in the weight ratio of ZO in the IS/ZO composites, there is a noticeable enhancement in the intensity of the diffraction peaks associated with the (100) and (110) planes of ZO. Importantly, the characteristic diffraction peaks of cubic IS are also clearly observed, indicating the coexistence of ZO and IS in the composite structure.

The surface areas, pore volumes, and pore diameters of the ZO, IS,

and 40 % ZO/IS composite photocatalysts were characterized through N₂ adsorption-desorption isotherms (Figs. 2b and c). Fig. 2b demonstrates that all samples exhibit Type IV adsorption-desorption isotherms, characteristic of mesoporosity [33]. Pure ZO shows an H4-type hysteresis loop, indicating the presence of uniform slit-shaped pores [33]. In contrast, the IS exhibits a H3-type hysteresis, indicative of mesoporous structures [34], consistent with the SEM observations. These mesoporous structures may have resulted from the assembly of nanosheets into nanoflowers or from gaps between nanoflakes observed in SEM images. The nitrogen adsorption-desorption isotherms of the 40 % ZO/IS composite resemble those of IS, suggesting that the incorporation of ZO particles negligibly impacts the IS structure. The specific surface area (S_{BET}) of IS (87.88 m²/g) surpasses the value of ZO (14.97 m²/g), as shown in Table S1. The S_{BET} of 40 %–ZO/IS falls below that of IS but exceeds the result of ZO. The reduction in surface area of the composite suggests that the enhancement in activity is not directly related to the surface area. The Barrett-Joyner-Halenda (BJH) method was used to determine the pore size distribution of ZO, IS, and the 40 %–ZO/IS composite photocatalysts (Fig. 2c). The results indicate that the average pore diameter of ZO/IS (10.78 nm) is smaller compared to the value of ZO (16.04 nm), but larger than that of bare IS (10.17 nm) (Fig. 2c). This observation aligns with the morphology analysis, suggesting that the incorporation of ZO does not interfere with the underlying hierarchical structure of IS.

Ultraviolet-visible diffuse reflectance spectroscopy (UV-Vis DRS) was employed to examine the light absorption characteristics of pure ZO, IS, and x %–ZO/IS composites (Fig. 2d). The absorption spectrum of pristine IS shows a distinct onset at approximately 650 nm, indicating a

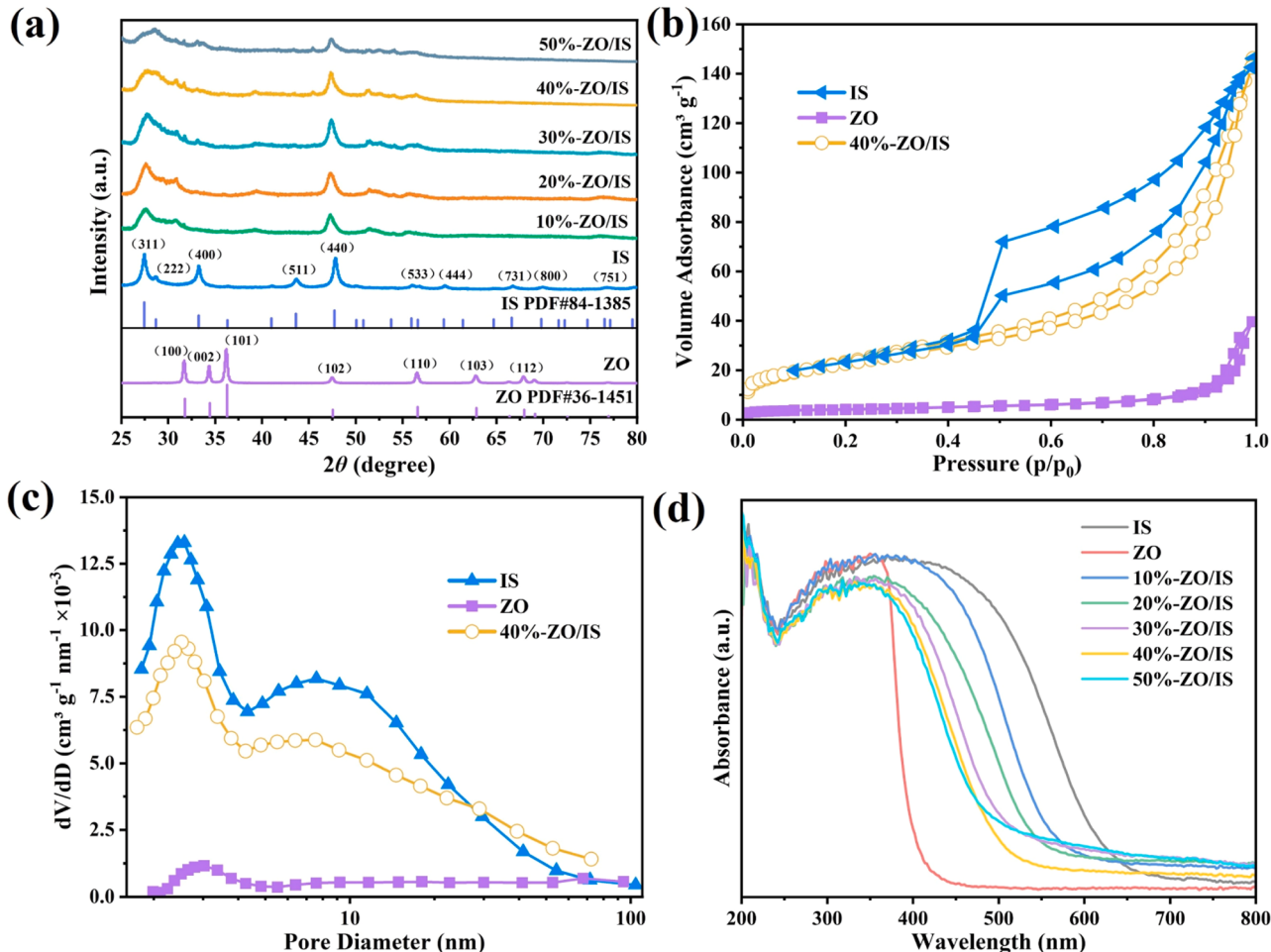


Fig. 2. (a) XRD patterns, (b) N₂ adsorption-desorption isotherms, (c) pore size distribution curves and (d) UV-vis spectra of IS, ZO, and x %–ZO/IS.

high reactivity to visible light for photocatalytic applications. Conversely, ZO displays a prominent absorption threshold around 400 nm, attributed to its wide bandgap [35]. Band gap energies (E_g) for the samples were estimated using Tauc plots, with IS exhibiting a value of 2.10 eV and ZO displaying 3.24 eV, as depicted in Fig. S2. Integrating ZO into the composites induces an absorption spectrum blue shift. Furthermore, a significant rise in ZO concentration markedly diminishes light absorption. This decline can be attributed to a decrease in the IS content. Consequently, the light absorption of ZO/IS composites is inferior to that of IS alone, suggesting that other factors, rather than light absorption, contribute to the enhanced photocatalytic performance of the composite.

3.2. Photocatalytic tetracycline hydrochloride degradation activity

In this study, we initially conducted the photodegradation of tetracycline hydrochloride (TCH), under Xenon lamp illumination, to evaluate the photocatalytic efficacy of the synthesized S-scheme ZO/IS materials. Fig. 3a shows minimal degradation of TCH in the absence of any photocatalyst. The S-scheme ZO/IS samples exhibited remarkable performance in the photodegradation of TCH, surpassing both IS and ZO. Fig. S3 shows that the 40 %-ZO/IS composite has the highest efficiency, resulting in 86 % TCH degradation within 120 minutes. Similar results were obtained upon replacing commercial ZO with the ZO sample synthesized in our laboratory (Fig. S4), confirming the

enhancement of the photocatalytic activity across diverse ZO synthesis methods. Table S2 provides a comparison of the photocatalytic TCH degradation activity of S-scheme ZO/IS with other recently documented photocatalysts [36–40], highlighting the exceptional efficiency of our material in eliminating antibiotics from aqueous solutions.

The plots depicting $-\ln(C/C_0)$ as a function of time are displayed in Fig. 3b, showing nearly linear curves for all samples. Fig. 3b also displays the kinetic constants (k) for the various samples. The k value of the 40 %-ZO/IS photocatalyst is 0.0150 min^{-1} , demonstrating a significant increase of 1.85 and 1.92 times, respectively, compared to pure IS (0.0081 min^{-1}) and ZO (0.0078 min^{-1}). Remarkably, the 40 %-ZO/IS photocatalyst outperforms the other x %-ZO/IS photocatalysts. The decrease in photocatalytic activity with higher ZO loading is likely attributed to reduced photoabsorption, resulting in a lower number of photogenerated carriers. Nevertheless, the S-scheme ZO/IS photocatalysts demonstrate efficiency in the degradation of TCH under Xenon light irradiation.

The reusability of the ZO/IS composite was investigated, as depicted in Fig. 3c. The photocatalytic efficiency achieves values of 86.0 %, 85.5 %, 85.0 % and 83.8 % during the first to fourth cycles, respectively, within a 120-min timeframe. However, a slight reduction in degradation efficiency is observed, possibly related to the presence of residual TCH and intermediates on the surface of the 40 %-ZO/IS after repeated cycles [41]. Moreover, an analysis of SEM images, XRD diffractograms and XPS spectra of both pristine and used 40 %-ZO/IS photocatalyst reveals that

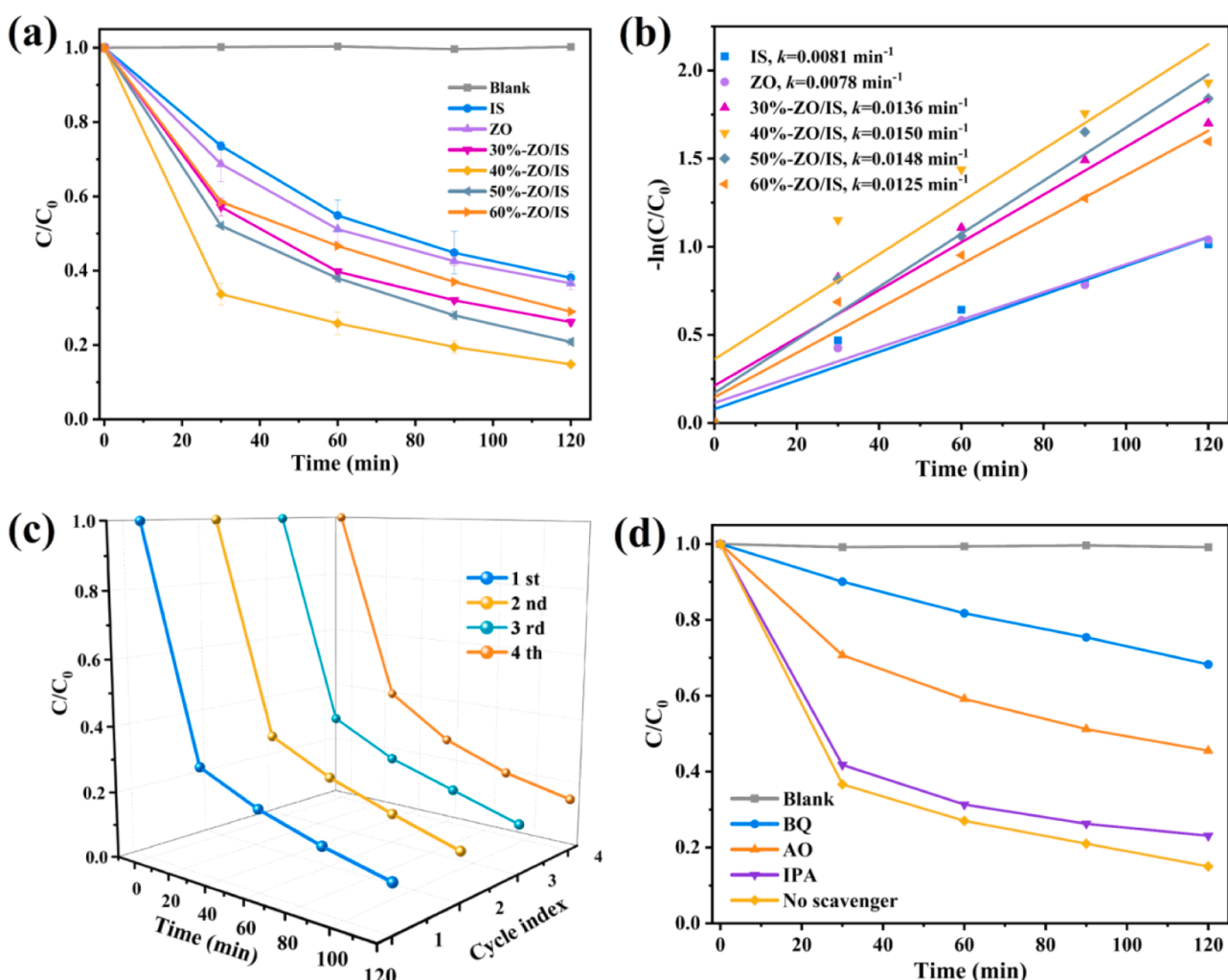


Fig. 3. (a) Photocatalytic degradation of TCH. (b) Pseudo-first-order reaction kinetics curves of TCH. (c) Cycle experiments for photodegradation of TCH over 40 %-ZO/IS. (d) Performance of 40 %-ZO/IS in the photocatalytic degradation of TCH in the presence of different scavengers.

the ZO and IS components remain within the composite after the photocatalytic reaction (Figs. S5–7), exhibiting minimal changes in terms of crystal structure, morphology, and chemical state, even after the photocatalytic degradation experiment. This highlights the chemical durability of the composite framework in the elimination of antibiotics from wastewater.

To elucidate the roles of active species in the reaction, the effects of different scavenging agents on the photocatalytic process were investigated. Specifically, 1,4-benzoquinone (BQ), ammonium oxalate (AO), and isopropanol (IPA) were employed as scavengers for $\bullet\text{O}_2^-$, h^+ and $\bullet\text{OH}$

[42], respectively. Fig. 3d illustrates that the addition of IPA minimally impacts the photocatalytic degradation efficiency of TCH. However, the degradation significantly diminishes with the introduction of AO and BQ. The inclusion of AO results in a reduction in the degradation rate of TCH from 86 % to 54 %, while the inclusion of BQ leads to a decrease from 86 % to 31 %. This suggests that h^+ and $\bullet\text{O}_2^-$ are the primary active species in the TCH photocatalytic degradation process, with $\bullet\text{O}_2^-$ having the most significant impact, followed by h^+ , and then $\bullet\text{OH}$. Additionally, the electron spin resonance (ESR) spectra (Figs. S8–10) demonstrate the presence of these active species, including DMPO- $\bullet\text{O}_2^-$, TEMPO- h^+ and

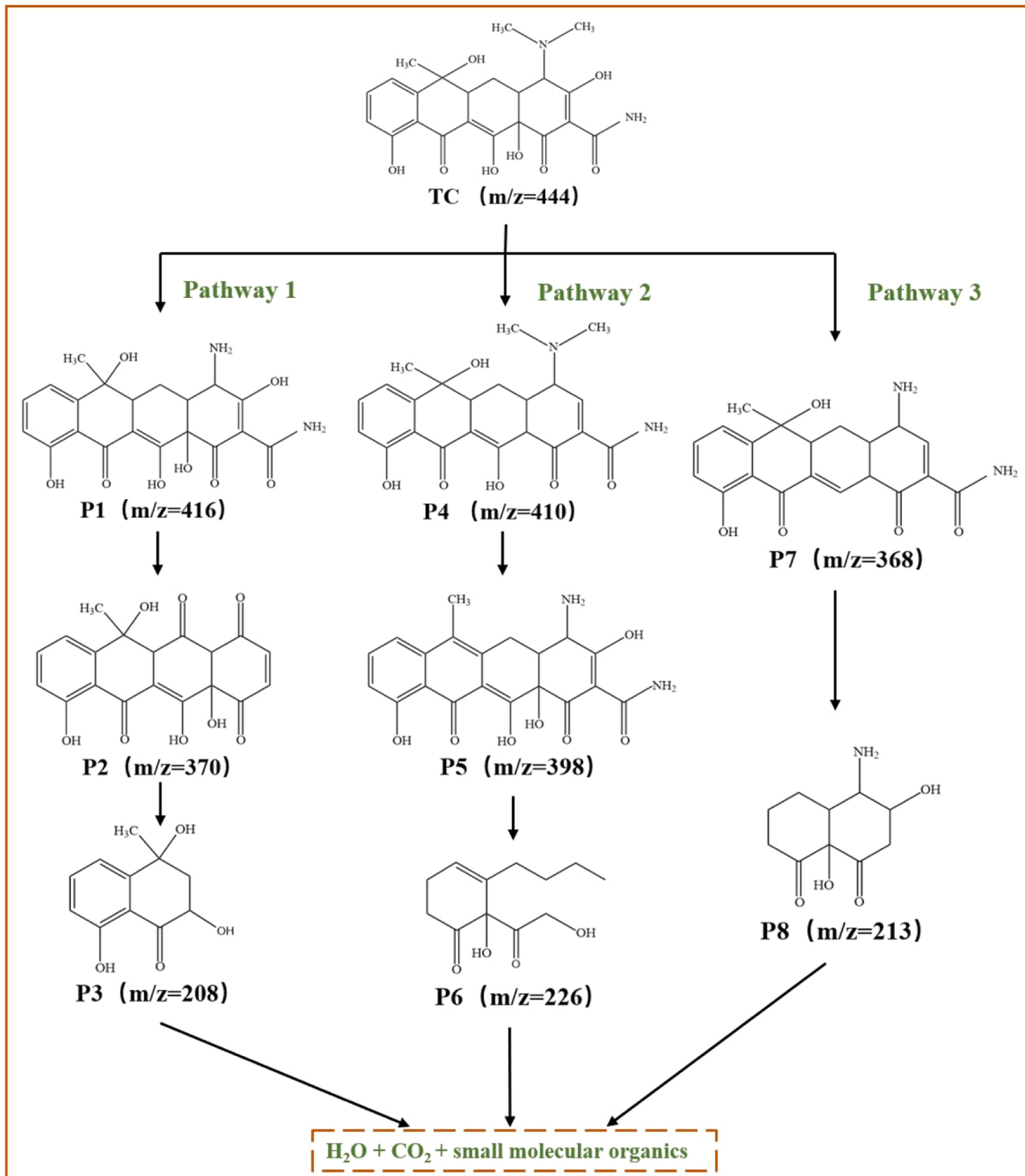


Fig. 4. Proposed photocatalytic degradation pathways.

•OH in 40 %-ZO/IS. Fig. S8 indicates the absence of •O₂ signal under dark conditions. After 5 minutes of illumination, a strong DMPO-•O₂ signal is evident in the 40 %-ZO/IS composite, surpassing the intensity of unmodified IS. This demonstrates an improvement of the photocatalytic effectiveness by •O₂. Additionally, when exposed to light for the same duration, there is a pronounced decrease in TEMPO-h⁺ intensity (Fig. S9), compared to darkness, denoting the crucial contribution of h⁺ to tetracycline degradation. Moreover, in the absence of light, no •OH signals are present; however, under illumination, distinct •OH peaks become evident (Fig. S10), indicating the generation of •OH during the photocatalytic process. Therefore, free radical capture experiments and ESR analysis demonstrate that the photocatalytic process is controlled by the combined action of free radicals •O₂, h⁺ and •OH.

To examine the degradation of TCH in the 40 %-ZO/IS system, intermediates were identified using HPLC-MS (Fig. S11). The primary degradation pathways for TCH are illustrated in Fig. 4. The MS spectrum in Fig. S12 shows the initial *m/z* value of 444, corresponding to the characteristic peak of TCH [43]. In pathway I, tetracycline undergoes demethylation (*m/z*=416) to form P1, followed by the conversion of carbonyl groups and the loss of amino, amide and hydroxyl groups, resulting in the formation of P2 (*m/z*=370) [43]. P2 is transformed into P3 when attacked by active species (*m/z*=208). In pathway II, the TCH molecule is subjected to the action of h⁺ and •O₂ radicals, leading to the elimination of two hydroxyl groups, forming P4 (*m/z*=410). Subsequently, P4 experiences demethylation and dehydroxylation reactions, resulting in the formation of P5 (*m/z*=398), which further undergoes oxidation and ring opening reactions to create P6 (*m/z*=226). On the

other hand, pathway III involves the demethylation and dehydroxylation of tetracycline, leading to the formation of P7 (*m/z*=368), which then goes through oxidation and ring opening to generate P8 (*m/z*=213). These intermediates decompose into H₂O, CO₂ and smaller by-products, under the influence of reactive species present in the photocatalytic system.

3.3. Photocatalytic hydrogen evolution performance

To further elucidate the catalytic properties of our sample catalysts, we conducted a photocatalytic H₂ evolution experiment. Fig. 5a compares the effectiveness of IS, ZO, and a 40 %-ZO/IS composite in generating H₂ under irradiation of Xe light, using triethanolamine (TEOA) as the hole scavenger. The H₂ production obtained with ZO/IS steadily increases with irradiation time, while pure IS exhibits a slow increase, and bare ZO shows almost no H₂ evolution. Fig. 5b presents the hydrogen production rates via photocatalysis for various specimens after 2 h of illumination. The data show that the microflower-like IS achieves a hydrogen generation rate of 71 μmol g⁻¹ h⁻¹, while the ZO sample produces hydrogen at a significantly lower rate of 6 μmol g⁻¹ h⁻¹, indicating limited photocatalytic efficiency in pure IS and ZO samples. Nevertheless, the establishment of a heterojunction results in a substantial enhancement in the capabilities of photocatalytic hydrogen production. The H₂ production rate initially increases with an increase in ZO content, peaking at 30 %, and then diminishes when the ZO content reaches 40 %. (Fig. 5b). In ZO/IS catalysts, excessive ZO can hinder the light absorption (shading effect) of IS or fail to provide

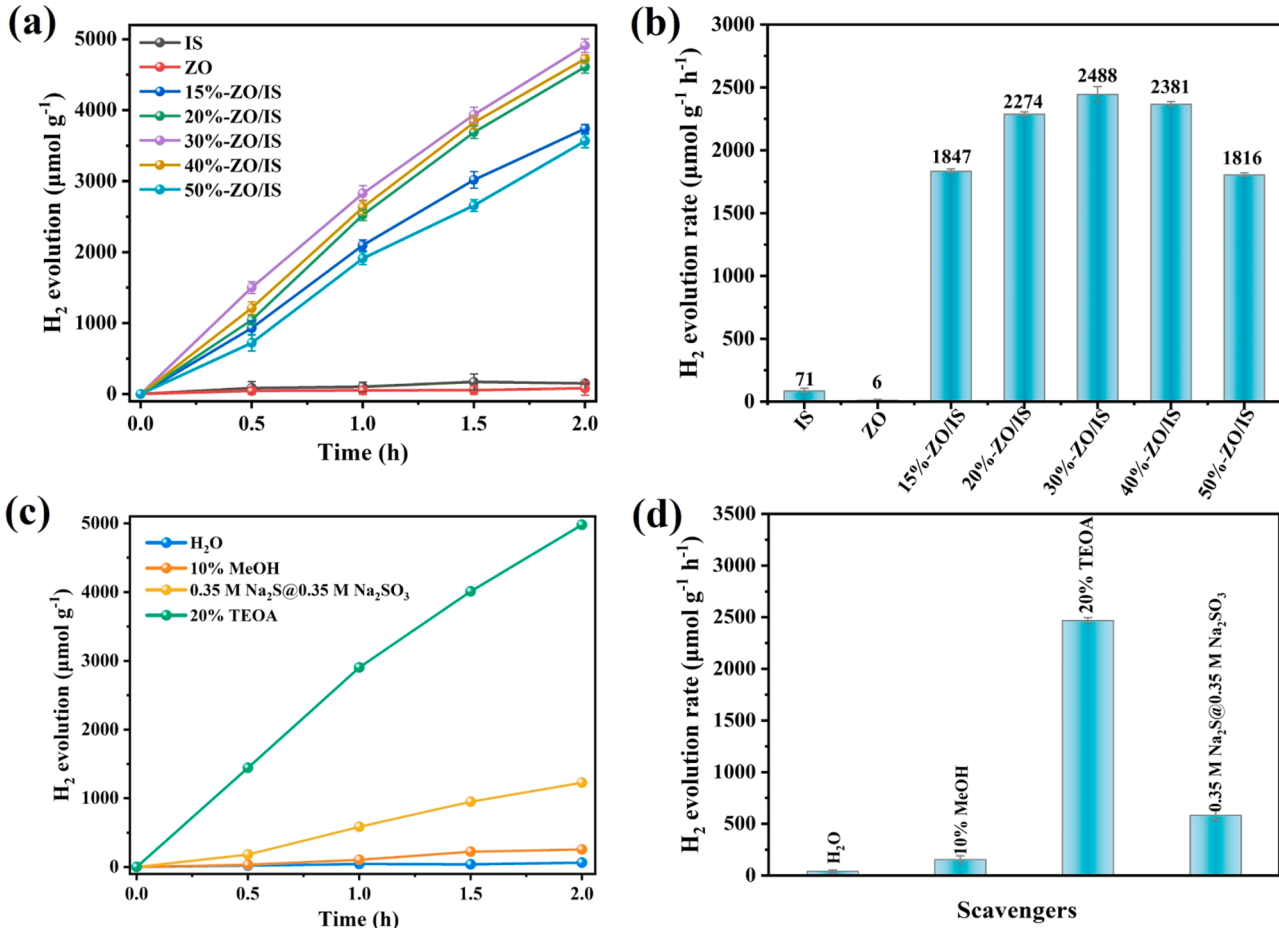


Fig. 5. (a) Time profiles of photocatalytic hydrogen generation of IS, ZO, and x %-ZO/IS composites under Xe irradiation. (b) Average H₂ production of IS, ZO, and x %-ZO/IS composites. (c) Photocatalytic H₂ production of 40 %-ZO/IS with different sacrificial agents. (d) Effect of different sacrificial agents on average H₂ production of 40 %-ZO/IS.

sufficient reactive sites, leading to a decline in photocatalytic performance [44]. The optimized 30 %–ZO/IS composite exhibits a hydrogen production rate of $2488 \mu\text{mol g}^{-1} \text{ h}^{-1}$, representing a 35-fold enhancement over the baseline IS. Additionally, the 40 % ZO/IS composite photocatalyst demonstrates an apparent quantum efficiency (AQE) of 11.35 % at 420 nm (Fig. S13). Furthermore, the composite photocatalyst developed in this study exhibits superiority compared to other photocatalysts based on IS or ZO, as shown in Table S3. Additionally, the comparison of photocatalytic activity between the prepared samples and state-of-the-art photocatalysts from literature is shown in Table S4. Consequently, ZO emerges as a particularly suitable choice for enhancing the photocatalytic efficacy of IS.

3.4. Photocatalytic mechanism

The photocatalytic performance of a semiconductor material is predominantly governed by its phase crystallinity, microstructure, surface area, light absorption, charge separation, and transfer efficiency [45, 46]. The above-mentioned characterizations confirm that the incorporation of ZO has negligible effects on the crystal structure of IS. However, it simultaneously decreases the surface area and light absorption capacity of IS. Consequently, the increased photocatalytic efficiency of the heterojunction is primarily attributed to the enhanced charge separation and transfer kinetics, rather than to changes in crystal structure, surface morphology, or light absorption capacity. Therefore, our subsequent investigation aimed at elucidating the impact of tightly bound

ZO/IS heterojunctions on the dynamics of carrier separation and transfer.

Initially, the recombination and separation dynamics of photoinduced electrons within photocatalysts were examined using photoluminescence spectra (PL) and time-resolved photoluminescence spectra (TRPL). Fig. 6a depicts the steady-state PL of IS and 40 %–ZO/IS. The latter reveals diminished intensities compared to IS alone, suggesting a meaningful reduction in charge-carrier recombination. Additionally, the TRPL spectra (Fig. 6b) provide insights into the lifetimes of charge carriers in IS and ZO/IS. The average lifetime (τ_A) of diverse photocatalysts is commonly estimated using the following equation: $\tau_A = \frac{A_1 \tau_1^2 + A_2 \tau_2^2}{A_1 \tau_1 + A_2 \tau_2}$, where τ_1 and τ_2 represent the short and long lifetimes, respectively [47]. The fitted parameters, including the τ_A values of 0.327 ns for IS and 1.016 ns for 40 %–ZO/IS, are displayed in Table S5. The prolonged carrier lifetime in the ZO/IS heterojunction indicates effective charge separation of photogenerated electrons and holes, thereby enhancing carrier longevity. This characteristic significantly contributes to the photocatalyst's enhanced activity.

The kinetics of charge transfer was further examined through electrochemical characterization. Analysis of the electrochemical impedance spectra (EIS) reveals that the Nyquist semicircle diameter of the 40 %–ZO/IS electrode is smaller compared to pure IS and ZO electrodes (Fig. 6c). This suggests a reduced resistance to electron transfer, enhancing the efficiency of migration and separation of photogenerated electrons [48]. To evaluate the electrocatalytic performance of the IS,

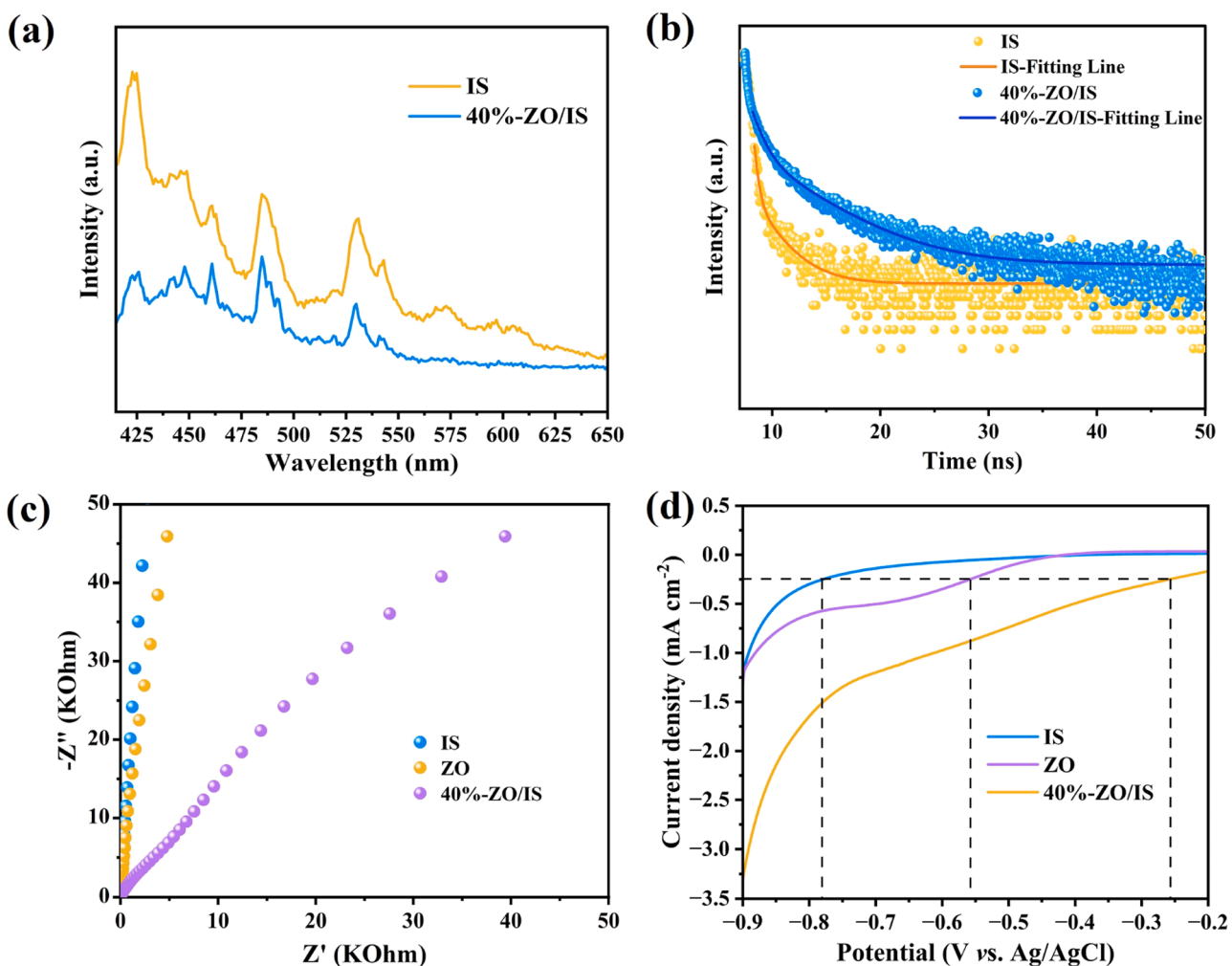


Fig. 6. (a) Photoluminescence spectra and (b) time-resolved photoluminescence decay spectra of IS and 40 %–ZO/IS. (c) EIS Nyquist plots and (d) current–voltage curves for proton reduction of IS, ZO, and 40 %–ZO/IS measured in the Na_2SO_4 solution.

ZO, and 40 %-ZO/IS electrodes in proton reduction, linear sweep voltammetry (LSV) tests were performed as shown in Fig. 6d. The current density observed on the 40 %-ZO/IS electrode surpasses that of the IS and ZO electrodes, demonstrating superior electrocatalytic activity for H₂ evolution on the ZO/IS surface. Additionally, the 40 %-ZO/IS electrode exhibits a lower overpotential (-0.26 V vs. Ag/AgCl) at a current density of -0.25 mA/cm² compared to the IS (-0.78 V vs. Ag/AgCl) and ZO (-0.56 V vs. Ag/AgCl) electrodes, demonstrating enhanced electrocatalytic hydrogen evolution with the ZO/IS composite.

Understanding the energy band structure is essential for elucidating the mechanism behind the increased activity in the ZO/IS heterojunction. The energy band structures for both IS and ZO photocatalysts were characterized by Mott-Schottky analysis, as illustrated in Figs. 7a and b. Analysis of the X-axis intercept reveals that the flat band potentials (E_{fb}) of IS and ZO are -0.7 V and 0 V (vs. NHE), respectively. Both IS and ZO Mott-Schottky curves exhibit positive tangent slopes, indicating n-type semiconductor behavior [49]. In n-type semiconductors, it is commonly observed that the conduction band potential (E_{CB}) is roughly 0.2 V below the E_{fb} [7]. Subsequently, we determined the E_{CB} values for IS and ZO to be -0.9 V and -0.2 V (vs. NHE), respectively. Using the relation $E_g = E_{VB} - E_{CB}$, where E_g denotes the band gap inferred from the Tauc plot, we determined the valence band potentials (E_{VB}) for IS and ZO to be 1.2 V and 3.04 V, respectively. The schematic diagrams in Fig. 7c and d depict the staggered band structures of IS and ZO, suggesting the possible emergence of a Type II or S-scheme

heterojunction.

If a type II heterojunction is present in the ZO/IS composite photocatalysts, the photogenerated electrons in the CB of IS will be transferred to the CB of ZO. This transportation is driven by the more positive potential of the CB of ZO ($E_{CB} = -0.2$ V) compared to that of IS ($E_{CB} = -0.9$ V). Furthermore, the migration of holes from the VB of ZO ($E_{VB} = +3.04$ V) to the VB of IS ($E_{VB} = +1.2$ V) occurs. The reduction reactions in the ZO/IS composite are facilitated by the CB electrons of ZO, which have an energy level of -0.2 V. On the other hand, the oxidation reactions are driven by the holes in the VB of IS, which have an energy level of +1.2 V. It is evident that the CB of ZO cannot thermodynamically reduce O₂ to •O₂⁻ (O₂/•O₂⁻, $E_0 = -0.33$ vs. NHE) [50], and the VB of IS cannot oxidize water molecules into •OH (H₂O/•OH, $E_0 = 2.38$ V; OH[•]/•OH, $E_0 = 1.99$ V vs. NHE) [51,52]. However, the superoxide trapping assays employing DMPO, as evidenced by Figs. S8 and S10, unambiguously reveal the presence of distinct •O₂⁻ and •OH signals within the ZO/IS composite. This finding effectively excludes the likelihood of a conventional type II heterojunction formation between ZO and IS.

Confirmation of the S-scheme heterojunction can be achieved through theoretical calculations, given the crucial role of the work function in determining electron transport in heterogeneous semiconductors. This allows the evaluation of the direction of charge transfer between type II or S-scheme charge transfer mechanisms. Figs. 8a and b shows that the work functions of ZO and IS are 7.5 and 5.1 eV,

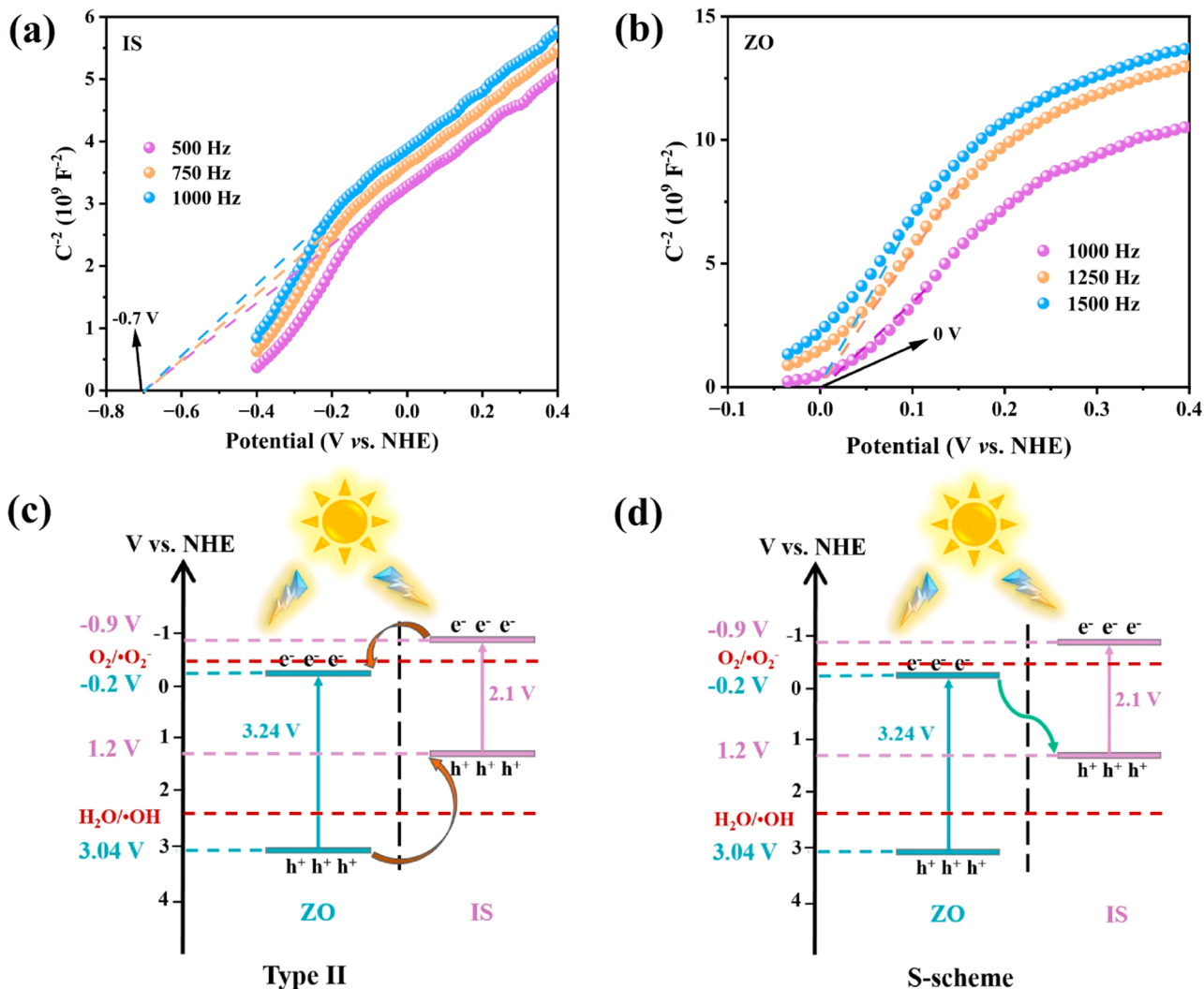


Fig. 7. Mott-Schottky curves of (a) IS and (b) ZO with different frequencies. (c) Type II heterojunction and (d) S-scheme heterojunction.

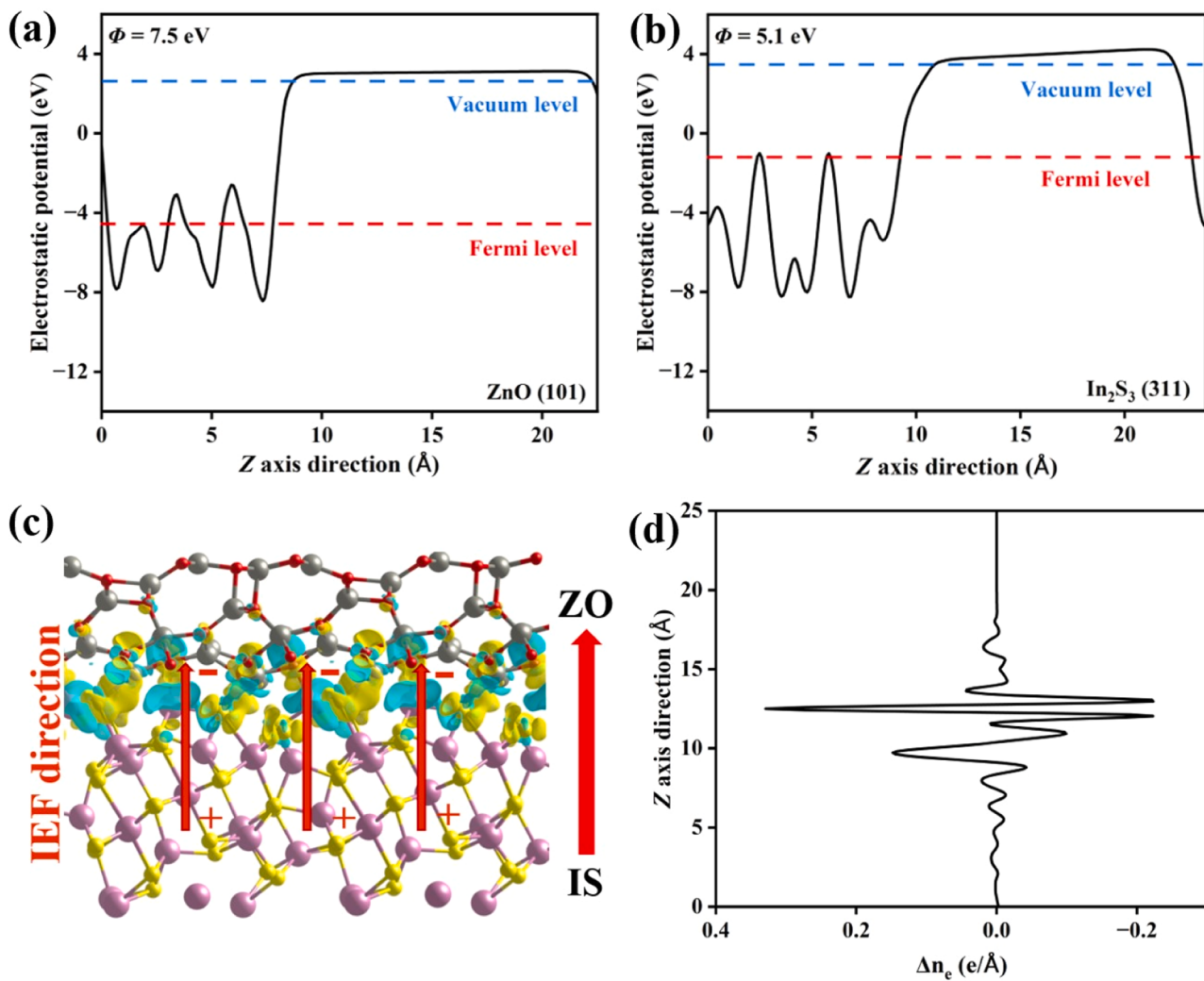


Fig. 8. (a-b) Work functions of ZO and IS. (c-d) 3D and planar averaged charge for the ZO/IS composite.

respectively, implying that electrons tend to migrate from IS to ZO upon contact, ultimately establishing a new Fermi level equilibrium state. The redistribution of charges at interfaces leads to the generation of an IEF between the negatively charged ZO and positively charged IS. When exposed to light, this electric field facilitates the transfer of photoelectrons from ZO to IS, consistent with the charge transfer mechanism described in the S-scheme. To provide further evidence of charge transfer at the ZO/IS interface, theoretical calculations for the 3D charge density and planar-averaged differential charge density were performed, as illustrated in Fig. 8c-d. The yellow regions indicate areas of charge accumulation, while the blue regions designate areas of charge depletion. Notably, the IS surface exhibits a frequent occurrence of the blue region at the interface with ZO. In contrast, the ZO surface displays multiple yellow regions and a comparatively limited amount of blue regions. These findings demonstrate the accumulation of electrons and negative charges on the ZO surface, as well as the buildup of holes and positive charges on the IS surface. Consequently, the existence of an IEF at the ZO/IS interface is confirmed, with the electric field directed from IS to ZO. These results further reinforce the formation of a S-scheme heterojunction between ZO and IS.

The experimental observation of charge transfer in the S-scheme ZO/IS interface was conducted under both dark and illuminated conditions using ex situ and *in situ* XPS techniques, as depicted in Fig. 9a. The XPS survey spectrum of the ZO/IS composite shows the presence of Zn, O, In, and S elements (Fig. S14). Fig. 9b displays the high-resolution In 3d

spectrum for unmodified IS with two distinct peaks at 451.0 and 443.4 eV, indicative of In 3d_{3/2} and In 3d_{5/2}, confirming the presence of In³⁺ [34]. Fig. 9c exhibits the high resolution spectra of S 2p, wherein two fitted peaks at 162.4 and 161.2 eV are ascribed to S 2p_{1/2} and S 2p_{3/2} of bare IS, respectively [15]. Fig. 9d depicts the presence of Zn²⁺ in bare ZO, as evidenced by the two peaks at binding energies of 1046.0 and 1023.0 eV, belonging to Zn 2p_{1/2} and Zn 2p_{3/2}, respectively [53]. Furthermore, Fig. 9e displays the fitted O 1 s spectrum of bare ZO, revealing two peaks assigned to Zn–O (530.7 eV) and –OH (532.5 eV), respectively [54,55]. Upon the formation of the ZO/IS heterojunction through the coupling of ZO with IS, the high-resolution XPS spectra of In 3d and S 2p for ZO/IS display a noticeable shift towards higher binding energies, in comparison to the values of IS. Furthermore, the high-resolution XPS spectra of Zn 2p and O 1 s for ZO/IS show a shift towards lower binding energies, in contrast to those for ZO. These results support the transfer of electrons from IS to ZO upon their combination in ZO/IS and indicate the presence of a space charge region at the interface between ZO and IS in ZO/IS, together with a built-in electric field pointing from IS to ZO.

The high-resolution S 2p spectrum of ZO/IS exhibits an additional peak at 162.5 eV, while the O 1s spectrum of ZO/IS displays an extra peak at 531.2 eV. These peaks are attributed to the presence of S–O bonds [56–58], indicating the existence of interfacial chemical bonding at the ZO/IS interface. To gain insight into the chemical bonds present in the material, FT-IR experiments were also conducted. The findings of the

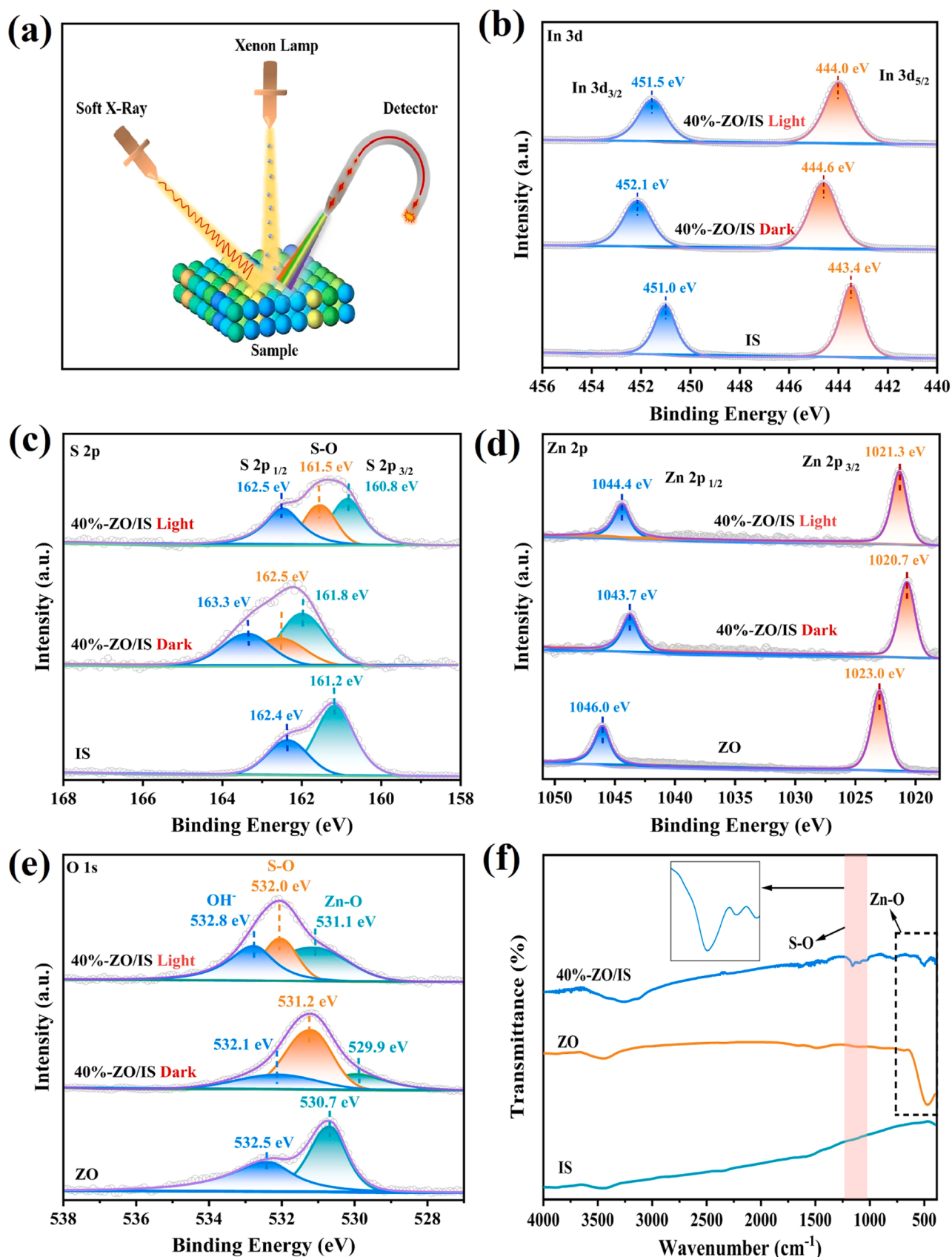


Fig. 9. (a) Schematic diagram of the *in situ* XPS apparatus. High-resolution XPS spectra of IS, ZO, and 40 %-ZO/IS composite with and without light irradiation: (b) In 3d, (c) S 2p, (d) Zn 2p and (e) O 1 s. (f) FT-IR spectra of IS, ZO, and 40 %-ZO/IS heterojunction.

FT-IR characterization on pure IS, ZO, and 40 %-ZO/IS heterojunction are depicted in Fig. 9f. In the bare ZO spectrum, the peak at 472 cm^{-1} can be assigned to the stretching vibrations of the Zn–O bonds [59,60]. In the spectrum of 40 %-ZO/IS, the presence of characteristic peaks corresponding to both IS and ZO confirms their coexistence in the heterojunction material. Furthermore, the identification of a new peak at 1055 cm^{-1} suggests the formation of strong chemical interactions through S–O bonds at the ZO/IS heterointerface, indicating the creation of covalent linkages between IS and ZO [56]. This interaction facilitates a fast electron migration and ensures the structural stability of the ZO/IS composite. These findings reveal the promising potential of the ZO/IS composite as a highly efficient photocatalyst, emphasizing the favorable interactions between ZO and IS facilitated by intense S–O bonding.

Furthermore, the *in situ* irradiated XPS technique enables a more in-depth investigation into the interface interactions and charge transfer pathways involved in the photocatalytic process using 40 %-ZO/IS. Under light excitation, the high-resolution XPS spectra show a distinct shift towards lower binding energies for the In 3d and S 2p peaks of ZO/IS, in contrast with ZO/IS without light excitation (Fig. 9b-c). This shift indicates the accumulation of photogenerated electrons on the surface of IS during light excitation. Moreover, the decrease in the binding energy of the S–O bond in Fig. 9c provides further evidence for the occurrence of photoproduced electron transfer through the S–O bond. Additionally, the Zn 2p (Fig. 9d) and O 1s (Fig. 9e) peaks in ZO/IS shift towards higher binding energy positions, when comparing the XPS data of 40 %-ZO/IS in the dark, suggesting the accumulation of photogenerated holes on the surface of ZO during light irradiation. It is further observed that the S–O bond undergoes a shift towards higher binding energies under irradiation, implying that the S–O bond acts as a pathway for electron transfer within the heterojunction. The above XPS findings provide crucial evidence regarding the direction of photoelectron flow in the 40 %-ZO/IS system, confirming the successful establishment of a S-scheme heterojunction between ZO and IS.

To visually observe interfacial charge transfer, KPFM was conducted. Fig. 10 displays the standard height image, contact potential difference (CPD) maps under both light and dark conditions, along with the corresponding CPD curves of IS and 40 %-ZO/IS, illuminated by Xe lamps. CPD variations along a straight line, both before and after illumination using IS and ZO/IS, are demonstrated in Fig. 10a4 and b4, respectively. Under dark conditions, the CPD distribution of IS ranges from -25.6 to

-8.8 mV , increasing to $950.5 - 970.7\text{ mV}$ for ZO/IS. The significant positive shift in the CPD value indicates electron depletion on the ZO/IS surface, consistent with S-scheme charge transfer under dark conditions. In this scheme, IS exhibits a higher Fermi level than ZO, leading to free electron transfer from IS to ZO and resulting in a higher CPD value in the ZO/IS composite. Importantly, the CPD value for the ZO/IS composite decreases upon light irradiation, indicating a reverse electron transfer, compared to the dark state. The observed phenomenon is attributed to the unique S-scheme heterojunction between the ZO and IS components. This junction facilitates the migration of a greater number of photo-generated electrons from ZO to IS, leading to increased electron accumulation on the surface of IS and, consequently, a reduction in the CPD. Additionally, the surface photovoltage can be determined by evaluating the contact potential difference (ΔCPD) between light and dark conditions. The ΔCPD value of ZO/IS (27.9 mV) is substantially larger than the 9.7 mV value of IS. These results indicate a considerable improvement in the generation of photogenerated carriers after light exposure in the ZO/IS system, consistent with the enhanced photocatalytic efficacy observed.

The formation of a heterojunction between ZO and IS in the ZO/IS system has been confirmed through our experimental characterization and theoretical calculations. The subsequent section provides a summary of mechanism underlying charge separation/transfer in the S-scheme heterojunction, as depicted in Fig. 11. Before contact, the band structure diagram of n-type ZO and n-type IS in their initial state is depicted in Fig. 11a. As the Fermi level (E_F) of IS exceeds that of ZO, electrons migrate from IS to ZO upon contact, as shown in Fig. 11b. This migration causes an upward bending of the CB and VB of IS, while the CB and VB of ZO, near the IS-ZO interface, experience a downward bending, ultimately reaching equilibrium. This process leads to the formation of a built-in electric field, as illustrated in Fig. 11b. When exposed to light, both IS and ZO generate electrons and holes (Fig. 11c). Subsequently, the photogenerated electrons from IS accumulate in the CB of IS, while the photoinduced holes are confined to the VB of ZO due to the robust built-in electric field and band bending at the interface of IS and ZO. Simultaneously, the ZO CB electrons recombine with the VB holes within IS, which are propelled by the same electric field. This process ensures the preservation of the elevated reduction capability of the photo-generated electrons in IS and improved oxidation capability of the photoinduced holes in ZO, respectively. As a result, the ZO/IS system

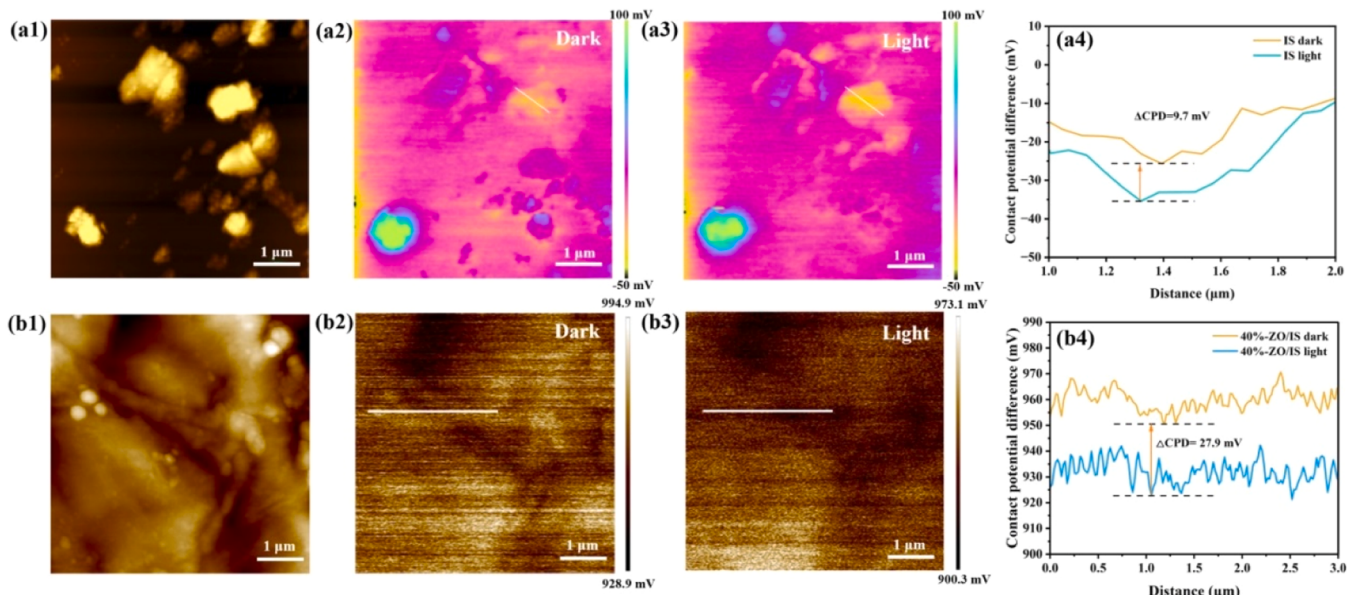


Fig. 10. (a1, b1) AFM images, (a2, a3, b2, b3) KPFM potential images and (a4, b4) the corresponding contact potential difference curves along the line in the dark and under illumination for (a1–a4) IS and (b1–b4) 40 % ZO/IS, respectively.

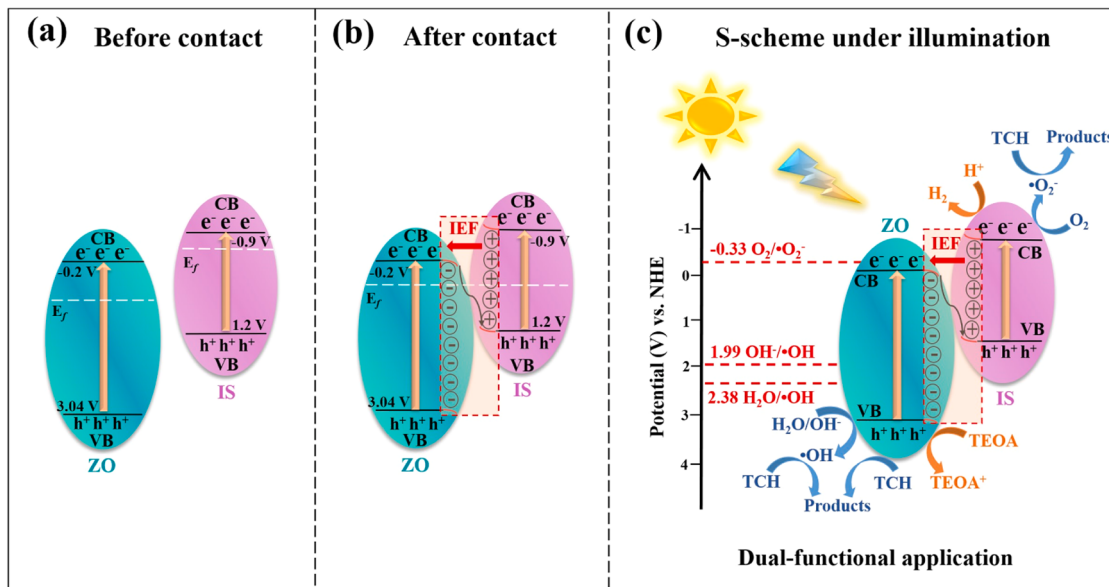


Fig. 11. Schematic representation of the charge transfer mechanism in the S-scheme ZO/IS heterostructure.

achieves high charge separation and transfer efficiency with elevated redox capacity.

Fig. 11c provides detailed insights to better elucidate the process of photocatalytic TCH photodegradation. The CB potential of the IS photocatalyst is -0.9 V vs. NHE, which is comparatively lower than the potential of $\text{O}_2/\bullet\text{O}_2$ (-0.33 V vs. NHE) [50]. Consequently, electrons can interact with O_2 on the surface of ZO/IS, leading to the formation of $\bullet\text{O}_2^-$. Additionally, the VB potential of ZO is measured to be 3.04 V vs. NHE, enabling the oxidation of H_2O to $\bullet\text{OH}$. Moreover, the h^+ species exhibit reactivity towards TCH, leading to direct attacks. HPLC-MS analysis (Fig. 4) confirms the involvement of $\bullet\text{O}_2^-$, $\bullet\text{OH}$ and h^+ in reactions with TCH, resulting in the formation of CO_2 , H_2O , and smaller molecules. Furthermore, the photocatalytic mechanism responsible for H_2 generation on the ZO/IS surface is also presented in Fig. 11c. The h^+ species retained in the valence band of ZO facilitate the oxidation of TEOA molecules through the S-scheme mechanism, while the electron-rich CB of IS reacts with H^+ to yield H_2 . Consequently, the implementation of this S-scheme yields a notable improvement in the dissociation of charges, leading to an enhancement in the photocatalytic efficacy for the production of hydrogen and the decomposition of TCH.

4. Conclusions

This study focuses on the synthesis of innovative S-scheme ZO/IS heterojunctions by incorporating commercially available ZO nanoparticles into the hydrothermal synthesis of IS. This method effectively promotes the development of an interfacial interaction between the S-O bonds of ZO and IS, resulting in enhanced stability of the heterojunction and the establishment of an atomic-level interfacial channel to facilitate efficient charge separation. The ZO/IS S-scheme heterojunction generates a durable internal electric field, maintaining the potent redox capabilities of photoexcited electrons and holes, while improving the efficiency of electron-hole separation by recombining photogenerated electrons and holes with lower redox abilities. Additionally, *in situ* XPS and KPFM analyses monitor the dynamic transfer of interfacial photogenerated electrons in the S-scheme, as evidenced by observable alterations in the binding energy and surface potential of ZO/IS. The utilization of the S-scheme charge transfer mechanism of the 40 % ZO/IS composite results in a notable degradation rate of 86 % of TCH after 2 h of light exposure. Moreover, the 30 % ZO/IS composite photocatalyst exhibits a hydrogen production rate of $2488 \mu\text{mol g}^{-1} \text{h}^{-1}$. Recycling experiments confirm the durability of the ZO/IS composite.

photocatalyst. This study verifies the potential for enhancing photocatalytic activity by constructing S-scheme heterojunctions with a strong internal electric field, introducing a pioneering methodology for creating efficient, economical, and long-lasting high-activity photocatalysts, specifically designed for the dual-functional application of environmental pollutant degradation and hydrogen production.

CRediT authorship contribution statement

Xianqiang Xiong: Writing – review & editing, Supervision, Resources, Project administration, Formal analysis, Conceptualization. **Sónia A.C. Carabineiro:** Writing – review & editing, Formal analysis. **Yating Ai:** Writing – original draft, Investigation, Formal analysis. **Jiajie Hu:** Writing – original draft, Formal analysis, Data curation. **Alexander Agafonov:** Formal analysis. **Kangle Lv:** Writing – review & editing, Formal analysis, Conceptualization. **Yuesheng Li:** Formal analysis. **Nikolay Sirokin:** Formal analysis.

Declaration of Competing Interest

The authors declare that they have no known competing financial interests or personal relationships that could have appeared to influence the work reported in this paper.

Data availability

Data will be made available on request.

Acknowledgments

The present study received financial support from the National Natural Science Foundation of China (22102112 & 51672312), Hubei Provincial Natural Science Foundation and Huangshi of China (2022CFD001), the Domestic Visiting Scholar “Teacher Professional Development Project” (FX2023052), the Zhejiang Provincial Natural Science Foundation of China (LQ21B030003), the “Pioneer” and “Leading Goose” R&D Program of Zhejiang (2023C03135), the Fundamental Research Funds for the Central Universities of South-Central Minzu University (CZP22001 & CZZ21012), and FCT/MCTES (Foundation for Science and Technology/Ministry of Science and Higher Education, Portugal, DOIs: 10.54499/CEECINST/00102/2018/CP1567/CT0026, 10.54499/LA/P/0008/2020, 10.54499/UIDB/

50006/2020 and 10.54499/UIDP/50006/2020).

Electronic supporting information

Supporting information is available in the online version of this article.

Appendix A. Supporting information

Supplementary data associated with this article can be found in the online version at doi:10.1016/j.apcatb.2024.124098.

References

- [1] S. Bao, Q. Tan, S. Wang, J. Guo, K. Lv, S.A.C. Carabineiro, L. Wen, TpBD COF@ZnIn₂S₄ nanosheets: a novel S-scheme heterojunction with enhanced photoreactivity for hydrogen production, *Appl. Catal. B* 330 (2023) 122624.
- [2] X. Xiang, L. Wu, J. Zhu, J. Li, X. Liao, H. Huang, J. Fan, K. Lv, Photocatalytic degradation of sulfadiazine in suspensions of TiO₂ nanosheets with exposed (001) facets, *Chin. Chem. Lett.* 32 (2021) 3215–3220.
- [3] J. Li, J. Yao, Q. Yu, X. Zhang, S.A.C. Carabineiro, X. Xiong, C. Wu, K. Lv, Understanding the unique Ohmic-junction for enhancing the photocatalytic activity of CoS₂/MgIn₂S₄ towards hydrogen production, *Appl. Catal. B* 351 (2024) 123950.
- [4] Z. Yu, K. Yang, C. Yu, K. Lu, W. Huang, L. Xu, L. Zou, S. Wang, Z. Chen, J. Hu, Y. Hou, Y. Zhu, Steering unit cell dipole and internal electric field by highly dispersed er atoms embedded into NiO for efficient CO₂ photoreduction, *Adv. Funct. Mater.* 32 (2022) 2111999.
- [5] R. Gao, H. He, J. Bai, L. Hao, R. Shen, P. Zhang, Y. Li, X. Li, Pyrene-benzothiadiazole-based polymer/CdS 2D/2D organic/inorganic hybrid S-scheme heterojunction for efficient photocatalytic H₂ Evolution, *Chin. J. Struct. Chem.* 41 (2022) 2206031–2206038.
- [6] P. Hu, Y. Xin, C. Yao, Y. Miao, In₂S₃/BiOI composites boost visible-light photocatalytic degradation of tetracycline hydrochloride, *CrystEngComm* 23 (2021) 3488–3497.
- [7] B. Guo, L. Bin, C. Wang, Y. Wang, S. Yin, W. Han, WS₂/In₂S₃ composite photocatalyst for photocatalytic H₂ generation and pollutant degradation, *N. J. Chem.* 46 (2022) 7366–7373.
- [8] R. Zhang, X. Jia, Y. Li, X. Yu, Y. Xing, Oxidation co-catalyst modified In₂S₃ with efficient interfacial charge transfer for boosting photocatalytic H₂ evolution, *Int. J. Hydrol. Energy* 47 (2022) 25300–25308.
- [9] W. Li, Y. Zhou, Q. Xu, X.-K. Wu, G.-D. Xu, J.-X. Guo, D. Fang, Fabrication of In₂S₃/MIL-68(Ind) heterojunction composite photocatalysts for degradation of Rhodamine B and hydrogen evolution, *J. Porous Mater.* 29 (2022) 181–192.
- [10] H. Cui, S. Dong, K. Wang, M. Luan, T. Huang, Synthesis of a novel Type-II In₂S₃/Bi₂MoO₆ heterojunction photocatalyst: excellent photocatalytic performance and degradation mechanism for Rhodamine B, *Sep. Purif. Technol.* 255 (2021) 117758.
- [11] R. Chen, Y. Huang, C. Rao, H. Su, Y. Pang, H. Lou, D. Yang, X. Qiu, Enhanced photocatalytic degradation of lignin by In₂S₃ with hydrophobic surface and metal defects, *Appl. Surf. Sci.* 600 (2022) 154110.
- [12] H. Li, Z. Yuan, C. Bittencourt, X. Li, W. Li, M. Chen, W. Li, R. Snyders, Anion exchange synthesis of hollow β-In₂S₃ nanoparticles: Adsorption and visible light photocatalytic performances, *J. Environ. Chem. Eng.* 7 (2019) 102910.
- [13] K. Li, S. Zhang, Y. Li, J. Fan, K. Lv, MXenes as noble-metal-alternative co-catalysts in photocatalysis, *Chin. J. Catal.* 42 (2021) 3–14.
- [14] C. Zhu, H. Yao, S. Le, Y. Yin, C. Chen, H. Xu, S. Wang, X. Duan, S-scheme photocatalysis induced by ultrathin TiO₂ (B) nanosheets-anchored hierarchical In₂S₃ spheres for boosted photocatalytic activity, *Compos. Part B Eng.* 242 (2022) 110082.
- [15] L. Yang, A. Li, T. Dang, Y. Wang, L. Liang, J. Tang, Y. Cui, Z. Zhang, S-scheme In₂S₃/ZnIn₂S₆ microsphere for efficient photocatalytic H₂ evolution with simultaneous photodegradation of bisphenol A, *Appl. Surf. Sci.* 612 (2023) 155848.
- [16] S. Li, K. Long, X. Sun, H. Yuan, W. Li, Activities in photocatalytic hydrogen evolution of In₂O₃/In₂S₃ heterostructure and In₂O₃/In₂S₃@PAN nanofibers, *Ceram. Int.* 49 (2023) 24093–24099.
- [17] Q. Li, L. Wang, J. Song, L. Zhang, C. Shao, H. Li, H. Zhang, Facile synthesis of hierarchical S-scheme In₂S₃/Bi₂WO₆ heterostructures with enhanced photocatalytic activity, *J. Environ. Chem. Eng.* 11 (2023) 109832.
- [18] L.Y. Zhang, J.J. Zhang, H.G. Yu, J.G. Yu, Emerging S-scheme photocatalyst, *Adv. Mater.* 34 (2022) 2107668.
- [19] M. Zhao, S. Liu, D. Chen, S. Zhang, S.A.C. Carabineiro, K. Lv, A novel S-scheme 3D ZnIn₂S₄/WO₃ heterostructure for improved hydrogen production under visible light irradiation, *Chin. J. Catal.* 43 (2022) 2615–2624.
- [20] H. Liu, C. Wu, K. Lv, D. Tang, Q. Li, In-situ generation of Au-carbon-TiO₂ Ohmic junction from Ti₃C₂ MXene for efficient photocatalytic H₂ evolution, *J. Mater. Sci. Technol.* 188 (2024) 144–154.
- [21] Q. Xu, L. Zhang, B. Cheng, J. Fan, J. Yu, S-scheme heterojunction photocatalyst, *Chem* 6 (2020) 1543–1559.
- [22] L. Wang, B. Cheng, L. Zhang, J. Yu, In situ irradiated XPS investigation on S-scheme TiO₂@ZnIn₂S₄ photocatalyst for efficient photocatalytic CO₂ reduction, *Small* 17 (2021) 2103447.
- [23] J. Bai, R. Shen, Z. Jiang, P. Zhang, Y. Li, X. Li, Integration of 2D layered CdS/WO₃ S-scheme heterojunctions and metallic Ti₃C₂ MXene-based Ohmic junctions for effective photocatalytic H₂ generation, *Chin. J. Catal.* 43 (2022) 359–369.
- [24] Z. Jiang, B. Cheng, L. Zhang, Z. Zhang, C. Bie, A review on ZnO-based S-scheme heterojunction photocatalysts, *Chin. J. Catal.* 52 (2023) 32–49.
- [25] N. Li, Y. Tian, J. Zhao, J. Zhang, W. Zuo, L. Kong, H. Cui, Z-scheme 2D/3D g-C₃N₄@ZnO with enhanced photocatalytic activity for cephalaxin oxidation under solar light, *Chem. Eng. J.* 352 (2018) 412–422.
- [26] S.I. Sinar Mashuri, M.F. Kasim, N.H. Mohd Kaus, Y.H. Tan, A. Islam, U. Rashid, N. Asikin-Mijan, J. Andas, Y.H. Taufiq-Yap, M.K. Yaakob, W.I.N. Wan Ismail, M. L. Ibrahim, Photo-response range extension of Z-scheme ZnO/CdS for LED-light-driven photo-active catalyst, *Renew. Sust. Energ. Rev.* 184 (2023) 113602.
- [27] Z. Xie, L. Xie, F. Qi, H. Liu, L. Meng, J. Wang, Y. Xie, J. Chen, C.-Z. Lu, Efficient photocatalytic hydrogen production by space separation of photo-generated charges from S-scheme ZnIn₂S₄/ZnO heterojunction, *J. Colloid Interface Sci.* 650 (2023) 784–797.
- [28] Y. Peng, B. Cheng, L. Zhang, J. Liu, J. Yu, In₂O₃/ZnO S-scheme heterojunction nanocomposite hollow microtubes with highly sensitive response to formaldehyde, *Sens. Actuators, B* 385 (2023) 133700.
- [29] Z. Qi, J. Chen, Q. Li, N. Wang, S.A.C. Carabineiro, K. Lv, Increasing the photocatalytic hydrogen generation activity of CdS nanorods by introducing interfacial and polarization electric fields, *Small* 19 (2023) 2303318.
- [30] B. He, P. Xiao, S. Wan, J. Zhang, T. Chen, L. Zhang, J. Yu, Rapid charge transfer endowed by interfacial Ni-O bonding in S-scheme heterojunction for efficient photocatalytic H₂ and imine production, *Angew. Chem. Int. Ed.* 62 (2023) e202313172.
- [31] Y. Hua, C. Hu, M. Arif, S.-M. Chen, M. Zhang, X. Liu, Direct Z-scheme WO₃/In₂S₃ heterostructures for enhanced photocatalytic reduction, Cr(VI), *J. Alloy. Compd.* 908 (2022) 164488.
- [32] J. Jiang, G. Wang, Y. Shao, J. Wang, S. Zhou, Y. Su, Step-scheme ZnO@ZnS hollow microspheres for improved photocatalytic H₂ production performance, *Chin. J. Catal.* 43 (2022) 329–338.
- [33] P. Madhusudan, Y. Wang, B.N. Chandrashekhar, W. Wang, J. Wang, J. Miao, R. Shi, Y. Liang, G. Mi, C. Cheng, Nature inspired ZnO/ZnS nanobranch-like composites, decorated with Cu(OH)₂ clusters for enhanced visible-light photocatalytic hydrogen evolution, *Appl. Catal. B* 253 (2019) 379–390.
- [34] M. Murugalakshmi, G. Mamba, V. Muthuraj, A novel In₂S₃/Gd₂O₃ p-n type visible light-driven heterojunction photocatalyst for dual role of Cr(VI) reduction and oxytetracycline degradation, *Appl. Surf. Sci.* 527 (2020) 146890.
- [35] T. Bi, Z. Du, S. Chen, H. He, X. Shen, Y. Fu, Preparation of flower-like ZnO photocatalyst with oxygen vacancy to enhance the photocatalytic degradation of methyl orange, *Appl. Surf. Sci.* 614 (2023) 156240.
- [36] J. Xu, B. Luo, W. Gu, Y. Jian, F. Wu, Y. Tang, H. Shen, Fabrication of In₂S₃/NaTaO₃ composites for enhancing the photocatalytic activity toward the degradation of tetracycline, *New J. Chem.* 42 (2018) 5052–5058.
- [37] K. Jia, G. Liu, D.-N. Lang, S.-F. Chen, C. Yang, R.-L. Wu, W. Wang, J.-D. Wang, Degradation of tetracycline by visible light over ZnO nanophotocatalyst, *J. Taiwan Inst. Chem. Eng.* 136 (2022) 104422.
- [38] X. Chen, S. Du, L. Gao, K. Shao, Z. Li, B. Liu, A hydrangea-like nitrogen-doped ZnO/BiOI nanocomposite for photocatalytic degradation of tetracycline hydrochloride, *Nanoscale Adv.* 5 (2023) 1936–1942.
- [39] M. Zhang, Z. Hou, W. Ma, X. Zhao, C. Ma, Z. Zhu, Y. Yan, C. Li, Fabrication of a visible-light In₂S₃/BiPO₄ heterojunction with enhanced photocatalytic activity, *N. J. Chem.* 42 (2018) 15136–15145.
- [40] H. Fan, H. Zhou, W. Li, S. Gu, G. Zhou, Facile fabrication of 2D/2D step-scheme In₂S₃/Bi₂O₃CO₃ heterojunction towards enhanced photocatalytic activity, *Appl. Surf. Sci.* 504 (2020) 144351.
- [41] H. Ren, F. Qi, A. Labidi, J. Zhao, H. Wang, Y. Xin, J. Luo, C. Wang, Chemically bonded carbon quantum dots/Bi₂WO₆ S-scheme heterojunction for boosted photocatalytic antibiotic degradation: Interfacial engineering and mechanism insight, *Appl. Catal. B* 330 (2023) 122587.
- [42] S. Liu, X. Jiang, G.I.N. Waterhouse, Z.-M. Zhang, L.-M. Yu, A novel Z-scheme NH₂-MIL-125(Ti)/Ti₃C₂ QDs/ZnIn₂S₄ photocatalyst with fast interfacial electron transfer properties for visible light-driven antibiotic degradation and hydrogen evolution, *Sep. Purif. Technol.* 294 (2022) 121094.
- [43] S. Fang, W. Zhang, K. Sun, Y.H. Hu, Highly efficient thermo-photocatalytic degradation of tetracycline catalyzed by tungsten disulfide under visible light, *Environ. Chem. Lett.* 21 (2023) 1287–1295.
- [44] K. Li, Y.-Z. Lin, Y. Zhang, M.-L. Xu, L.-W. Liu, F.-T. Liu, Boosting the photocatalytic activity of graphite carbon nitride by designing novel MoS₂-transition metal heterojunction cocatalysts, *J. Mater. Chem. C* 7 (2019) 13211–13217.
- [45] J. Li, Q. Yu, X. Zhang, X. Xiong, Y. Jin, D. Han, B. Yu, J. Yao, G. Dai, Coupling CoS₂ and CaIn₂S₄ for efficient electron trapping and improved surface catalysis to promote solar hydrogen evolution, *Int. J. Hydrogen Energy* 51 (2024) 314–326.
- [46] Z. Yan, X. Zhang, B. Yu, J. Yao, D. Han, Y. Jin, C. Wu, G. Dai, X. Xiong, Integrating CaIn₂S₄ nanosheets with Co₃O₄ nanoparticles possessing semiconducting and electrocatalytic properties for efficient photocatalytic H₂ production, *Ceram. Int.* 50 (2024) 3052–3063.
- [47] S. Le, Y. Ma, D. He, X. Wang, Y. Guo, CdS/NH₄V₄O₁₀ S-scheme photocatalyst for sustainable photo-decomposition of amoxicillin, *Chem. Eng. J.* 426 (2021) 130354.
- [48] K. Huang, G. Liang, S. Sun, H. Hu, X. Peng, R. Shen, X. Li, Interface-induced charge transfer pathway switching of a Cu₂O-TiO₂ photocatalyst from p-n to S-scheme heterojunction for effective photocatalytic H₂ evolution, *J. Mater. Sci. Technol.* 193 (2024) 98–106.

- [49] L. Gnanasekaran, W.-H. Chen, M. Soto-Moscoso, Highly operative NiO/ZnO nanocomposites for photocatalytic removal of azo dye, *Chemosphere* 308 (2022) 136528.
- [50] R. Mu, Y. Ao, T. Wu, C. Wang, P. Wang, Synthesis of novel ternary heterogeneous anatase-TiO₂ (B) biphase nanowires/Bi₄O₅I₂ composite photocatalysts for the highly efficient degradation of acetaminophen under visible light irradiation, *J. Hazard. Mater.* 382 (2020) 121083.
- [51] J. Zhang, Z. Ma, Ag-Ag₃VO₄/AgI₀₃ composites with enhanced visible-light-driven catalytic activity, *J. Colloid Interface Sci.* 524 (2018) 16–24.
- [52] W. Shi, F. Guo, S. Yuan, In situ synthesis of Z-scheme Ag₃PO₄/CuBi₂O₄ photocatalysts and enhanced photocatalytic performance for the degradation of tetracycline under visible light irradiation, *Appl. Catal. B* 209 (2017) 720–728.
- [53] J. Das, S.K. Pradhan, D.R. Sahu, D.K. Mishra, S.N. Sarangi, B.B. Nayak, S. Verma, B. K. Roul, Micro-Raman and XPS studies of pure ZnO ceramics, *Phys. B* 405 (2010) 2492–2497.
- [54] Y. Xu, H. Li, B. Sun, P. Qiao, L. Ren, G. Tian, B. Jiang, K. Pan, W. Zhou, Surface oxygen vacancy defect-promoted electron-hole separation for porous defective ZnO hexagonal plates and enhanced solar-driven photocatalytic performance, *Chem. Eng. J.* 379 (2020) 122295.
- [55] F. Rouzafzay, R. Shidpour, M.Z.M. Al-Abri, F. Qaderi, A. Ahmadi, M.T.Z. Myint, Graphene@ZnO nanocompound for short-time water treatment under sun- simulated irradiation: Effect of shear exfoliation of graphene using kitchen blender on photocatalytic degradation, *J. Alloy. Compd.* 829 (2020) 154614.
- [56] Y. Zhang, Y. Huang, S.-S. Zhu, Y.-Y. Liu, X. Zhang, J.-J. Wang, A. Braun, Covalent S-O bonding enables enhanced photoelectrochemical performance of Cu₂S/Fe₂O₃ heterojunction for water splitting, *Small* 17 (2021) 2100320.
- [57] H. Chai, L. Gao, P. Wang, F. Li, G. Hu, J. Jin, In₂S₃/F-Fe₂O₃ type-II heterojunction bonded by interfacial S-O for enhanced charge separation and transport in photoelectrochemical water oxidation, *Appl. Catal. B* 305 (2022) 121011.
- [58] C. Ding, Y. Lu, J. Guo, W. Gan, S. Qi, Z. Yin, M. Zhang, Z. Sun, Internal electric field-mediated sulfur vacancies-modified-In₂S₃/TiO₂ thin-film heterojunctions as a photocatalyst for peroxymonosulfate activation: Density functional theory calculations, levofloxacin hydrochloride degradation pathways and toxicity of intermediates, *Chem. Eng. J.* 450 (2022) 138271.
- [59] O. Dlugosz, M. Banach, Continuous synthesis of photocatalytic nanoparticles of pure ZnO and ZnO modified with metal nanoparticles, *J. Nanostruct. Chem.* 11 (2021) 601–617.
- [60] M. Samadi, H.A. Shivaee, M. Zanetti, A. Pourjavadi, A. Moshfegh, Visible light photocatalytic activity of novel MWCNT-doped ZnO electrospun nanofibers, *J. Mol. Catal. A: Chem.* 359 (2012) 42–48.